Large-Scale Semi-Passive RIS-Assisted Off-Grid DOA Estimation: A Quadratic Interpolation Method

Qi Yuan, Xinlei Shi, *Graduate Student Member, IEEE*, Xiaofei Zhang, and Fuhui Zhou, *Senior Member, IEEE*

***Abstract*—In this article, we propose a novel off-grid direction-of-arrival (DOA) estimation method in large-scale semi-passive reconfigurable intelligent surface (RIS) environments, utilizing quadratic interpolation techniques. Traditional DOA estimation methods, such as multiple signal classification (MUSIC) and atomic norm minimization (ANM), often struggle with the inherent complexities and limitations posed by extensive RIS deployments and off-grid targets. Our method effectively leverages the advantages of quadratic interpolation to enhance the DOA estimation accuracy while maximizing the utilization of available degrees-of-freedom (DOFs) from passive reflecting elements (PREs). We demonstrate that the proposed method can accurately estimate a larger number of targets in challenging scenarios when the number of active sensing elements (ASEs) is small. Furthermore, our method shows reduced computational complexity compared to conventional MUSIC and ANM methods, making it an efficient solution suitable for real-time applications. Extensive numerical simulations validate the efficacy of the proposed method, showcasing its capabilities in addressing off-grid errors and yielding high precision in DOA estimation. Overall, the findings highlight that our quadratic interpolation-based approach serves as a significant advancement in semi-passive RIS-assisted DOA estimation, preparing the ground for potential applications in next-generation wireless communication systems and smart sensor technologies.**

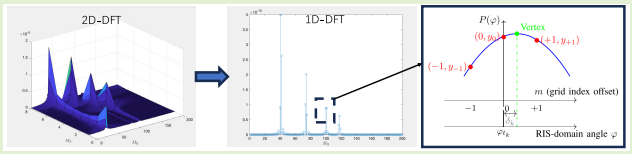

***Index Terms*— Direction-of-arrival (DoA) estimation, off-grid, semi-passive reconfigurable intelligent surface (RIS).**

I. Introduction

With the rapid evolution toward sixth-generation (6G) wireless networks, integrated sensing capabilities are expected to play a pivotal role in enabling environment-aware and intelligent applications [1], [2], [3], [4], [5]. In particular, low-complexity and high-accuracy sensing solutions are crucial for a wide range of sensor-based services, including smart transportation, industrial monitoring, and human activity recognition. However, conventional cellular base station (BS)-assisted sensing systems face inherent limitations, such as coverage blind spots and degraded performance in nonline-of-sight (NLOS) scenarios. These shortcomings stem from sparse BS deployment and severe signal blockages, which restrict reliable sensing and detection in complex propagation environments.

Reconfigurable intelligent surface (RIS) technology has emerged as a promising solution to mitigate these challenges [6], [7], [8]. By utilizing a large array of passive reflecting elements (PREs) to establish NLOS links, RIS can effectively reduce dead zones, alleviate signal interference, and enhance coverage through superior beamforming [9], [10], [11], [12]. Despite these advantages, RIS-assisted sensing faces challenges due to severe path loss; the BS-RIS-target-RIS-BS link experiences considerably more attenuation than traditional BS-target-BS links. To address this issue, semi-passive RIS integrates PREs with active sensing elements (ASEs), which directly capture target echoes and thus bypass the path losses associated with the RIS-BS link [13], [14], [15].

Direction-of-arrival (DOA) estimation is vital for effective target sensing when employing sparse BS deployments [16], [17], [18], [19], [20]. Recent approaches, such as the beam scanning protocol proposed in [21], aim to enhance RIS-assisted systems, yet they are limited to single-target scenarios. The work in [22] extends DOA estimation to multiple targets using the multiple signal classification (MUSIC) method, a well-established subspace-based method. However,

Received 14 November 2025; accepted 6 December 2025. Date of publication 18 December 2025; date of current version 2 February 2026. This work was supported in part by China NSF under Grant 62427801 and Grant 62371225, in part by the Major Achievements Cultivation Project under Grant NC2025010, and in part by the 407th Shuangqing Forum of the National Natural Science Foundation of China under Grant NQ2025005. The associate editor coordinating the review of this article and approving it for publication was Prof. Engin Masazade. *(Corresponding author: Xinlei Shi.)*

The authors are with the College of Electronic and Information Engineering and the Key Laboratory of Dynamic Cognitive System of Electromagnetic Spectrum Space, Ministry of Industry and Information Technology, Nanjing University of Aeronautics and Astronautics, Nanjing 211106, China (e-mail: yuanqi@nuaa.edu.cn; lincoln@nuaa.edu.cn; zhangxiaofei@nuaa.edu.cn; zhoufuhui@nuaa.edu.cn).

Digital Object Identifier 10.1109/JSEN.2025.3643411

1558-1748 © 2025 IEEE. All rights reserved, including rights for text and data mining, and training of artificial intelligence and similar technologies. Personal use is permitted, but republication/redistribution requires IEEE permission.
See https://www.ieee.org/publications/rights/index.html for more information.
Authorized licensed use limited to: Christopher Newport University. Downloaded on February 23,2026 at 12:29:37 UTC from IEEE Xplore. Restrictions apply.

it fails to utilize the angular information embedded in PREs, which can limit its performance. Recognizing that PREs inherently encode target angles through phase shifts, incorporating this information is essential for improving estimation accuracy. To address this, [23] introduces an atomic norm minimization (ANM)-based approach that integrates both PRE and ASE information, formulating DOA estimation as a sparse signal reconstruction problem. While this method achieves near-optimal accuracy by approaching the Cramér–Rao bound with a discrete Fourier transform (DFT) measurement matrix, its computational complexity poses a significant challenge for large-scale and real-time applications. Furthermore, the grid search methods employed in [22] and [23] do not effectively address the off-grid problem, limiting their practical applicability.

To overcome these limitations, we propose a novel DOA estimation method based on quadratic interpolation for semi-passive RIS systems. Unlike conventional quadratic or higher order interpolation schemes in classical spectral estimation [24], [25], [26], [27], which generally assume a fully active array with complete channel observations, the proposed quadratic interpolation-based off-grid correction is specifically designed for the hybrid sensing characteristics of semi-passive RIS-assisted systems. In this architecture, only ASEs can perform direct measurements, while the remaining PREs contribute indirectly through controlled reflection. The proposed method jointly exploits the reflected signals induced by PREs together with the direct measurements from ASEs, thereby enabling effective off-grid correction under partial and mixed observation constraints. In addition, the quadratic interpolation stage is analytically refined to account for the spatial-frequency coupling introduced by the RIS structure, an effect that does not occur in conventional fully active array configurations. Through these tailored modifications, the proposed method achieves higher resolution and improved robustness in semi-passive RIS scenarios, where standard subgrid refinement methods often suffer from performance degradation due to incomplete information process. The contributions of this article are summarized as follows.

1) Conventional DOA estimation methods in semi-passive RIS systems primarily focus on ASEs, neglecting the crucial angular information embedded in PREs. Our method fully leverages both PREs and ASEs, significantly improving estimation accuracy.
2) Conventional DOA estimation methods, such as grid-based MUSIC and convex optimization-based ANM, suffer from substantial computational complexity when employing large-scale RIS deployments. Our method provides a closed-form solution that avoids grid search or iterative optimization, enhancing computational efficiency.
3) The proposed method effectively tackles off-grid errors, which are frequently encountered in conventional DOA estimation methods. By employing a quadratic interpolation method, our solution achieves subgrid DOA estimation accuracy while maintaining low computational complexity.

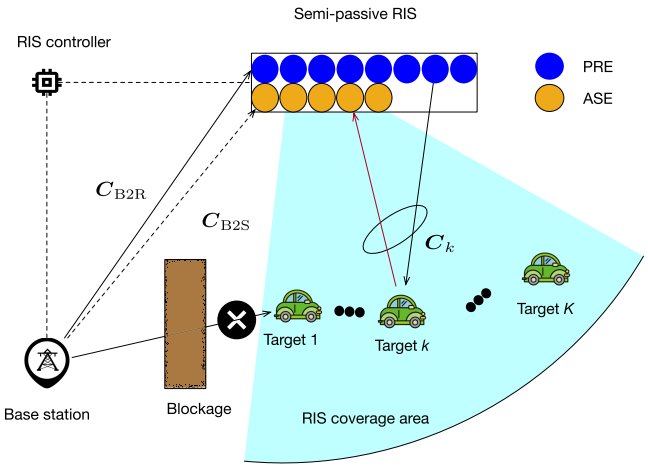

Fig. 1. Scene of semi-passive RIS-assisted sensing.

4) Theoretical analyses, including the mean squared error (mse) analysis of the estimator and complexity evaluation, are presented. Extensive simulations demonstrate that the proposed method achieves subgrid accuracy with significantly lower runtime compared to both ANM and MUSIC methods, thereby confirming its efficiency and robustness.

The rest of this article is organized as follows. Section II introduces the model formulation. The proposed method is derived in Section III. Sections IV and V present performance analysis and simulation results, respectively. Finally, conclusions are drawn in Section VI.

Throughout this article, vectors and matrices are represented by lower case bold and upper case bold letters, respectively; $(\cdot)^*$, $(\cdot)^T$, $(\cdot)^H$ denote conjugate, transpose, and Hermitian transpose operators, respectively; $\mathrm{diag}\{x_m\}_{m=1}^M$ denotes a $M \times M$ diagonal matrix with diagonal entries $x_1, x_2, \ldots, x_M$; $\|\cdot\|_2$ represents the l_2 norm; $\|\cdot\|_F$ represents the Frobenius norm; $\mathbb{E}[\cdot]$ is the statistical expectation operator; $\boldsymbol{I}_N$ is the $N \times N$ identity matrix; $\mathrm{Var}(x)$ denotes the variance of x; $\delta_{i,j}$ is the Dirac delta (=1 if $i = j$, and =0 otherwise); $\Re\{\cdot\}$ extracts the real part of a complex number; $|\cdot|$ means the modulus of a complex number; $\hat{a}$ denotes the estimate of a; $\mathbf{0}$ is the zero matrix or vector.

II. Model Formulation

Consider a semi-passive RIS-assisted sensing scenario illustrated in Fig. 1, where a BS equipped with M_B antennas aims to estimate the DOA of K targets. In the absence of line-of-sight (LOS) propagation, an RIS is employed to establish NLOS links that facilitate accurate DOA estimation.[1] The RIS consists of M_R PREs for phase adjustment and M_S ASEs for signal processing, resulting in enhanced sensing performance compared to fully passive RIS systems [13].

A. Channel Model

We assume a quasi-static flat-fading channel model for the time slots under consideration. For brevity, we consider

[1]We assume complete blockage of the LOS link to emphasize the RIS's critical role in enabling the sensing link.

Authorized licensed use limited to: Christopher Newport University. Downloaded on February 23,2026 at 12:29:37 UTC from IEEE Xplore. Restrictions apply.

that the BS, PREs, and ASEs are all organized as uniform linear arrays (ULAs) with half-wavelength spacing between elements. Additionally, the BS-PREs channel is modeled based on LOS propagation [23]

$$\boldsymbol{C}_{B2R} = \alpha_{B2R}\boldsymbol{a}_R(\theta_{B2R})\,\boldsymbol{a}_B^H(\vartheta_{B2R}). \tag{1}$$

Here, $\alpha_{B2R} = \lambda/(4\pi d_{B2R})e^{-j2\pi d_{B2R}/\lambda}$ represents the complex path gain, where λ is the carrier wavelength and d_{B2R} denotes the distance between the BS and RIS.[2] The angles ϑ_{B2R} and θ_{B2R} denote the BS's departure direction and the DOA at the PREs, respectively. The array response vectors for the PREs and BS are indicated as $\boldsymbol{a}_R(\cdot)$ and $\boldsymbol{a}_B(\cdot)$. For a ULA oriented at angle θ, the ith element of the response vector is expressed as $e^{j(i-1)\pi\sin\theta}$, where j represents the imaginary unit.

For brevity, we omit the channel between the BS and the ASEs, represented as $\boldsymbol{C}_{B2S}$ in Fig. 1 [21], [23], [28]. The channel from the PREs to target k and the ASEs is given by

$$\boldsymbol{C}_k = \alpha_k\boldsymbol{a}_S(\theta_k)\,\boldsymbol{a}_R^H(\theta_k) \tag{2}$$

where θ_k is the DOA of target k, and $\boldsymbol{a}_S(\cdot)$ represents the array response of ASEs. The path gain for the PREs-target k-ASEs channel is expressed as $\alpha_k = \lambda\gamma_k^{0.5}/8\pi^{1.5}d_k^2e^{(-j4\pi d_k)/\lambda}$ [23], where d_k refers to the distance from the RIS to target k, and γ_k is the radar cross section of target k [28]. We assume that the targets are located in the far-field of the RIS.

B. Sensing Model

To detect the targets, the RIS needs to scan various directions by adjusting its beams. We assume that the beam is modified for each snapshot, resulting in a total of T snapshots. The phase shift vector of the RIS at the tth snapshot is defined as $\boldsymbol{\phi}(t) = [e^{j\phi_1(t)}, e^{j\phi_2(t)}, \ldots, e^{j\phi_{M_R}(t)}]^T$, where $e^{j\phi_i(t)}$ represents the phase shift applied at the ith PRE. The echo signal received by the ASEs during the tth snapshot can be formulated as [23]

$$\boldsymbol{x}(t) = \sigma_t\sum_{k=1}^{K}\boldsymbol{C}_k\mathrm{diag}\left\{e^{j\phi_i(t)}\right\}_{i=1}^{M_R}\boldsymbol{C}_{B2R}\boldsymbol{h}s(t) + \boldsymbol{n}(t) \tag{3}$$

where σ_t^2 denotes the transmit power of BS; $s(t)$ is the transmitted signal; $\boldsymbol{n}(t) \sim \mathcal{CN}(0, \sigma_n^2\boldsymbol{I}_{M_S})$ is the additive white Gaussian noise; and $\boldsymbol{h}$ represents the beamforming vector of the BS, with $\|\boldsymbol{h}\|_2^2 = 1$. To maximize the power received by ASEs, the BS should direct its beam toward the RIS, specifically $\boldsymbol{h} = 1/\sqrt{M_B}\boldsymbol{a}_B(\vartheta_{B2R})$, resulting in

$$\boldsymbol{x}(t) = \sum_{k=1}^{K}\beta_k\boldsymbol{a}_S(\theta_k)\,\boldsymbol{a}_R^H\left(\tilde{\theta}_k\right)\boldsymbol{\phi}(t)\,s(t) + \boldsymbol{n}(t) \tag{4}$$

where $\tilde{\theta}_k = \arcsin(\sin\theta_k - \sin\theta_{B2R})$ and $\beta_k = \sqrt{M_B}\sigma_t\alpha_{B2R}\alpha_k$. By stacking the received echo signals across T snapshots, we obtain

$$\boldsymbol{X} \triangleq [\boldsymbol{x}(1), \boldsymbol{x}(2), \ldots, \boldsymbol{x}(T)] = \boldsymbol{A}_S\boldsymbol{\Lambda}\boldsymbol{A}_R^H\boldsymbol{D} + \boldsymbol{N} \tag{5}$$

[2]Since the BS and RIS are typically installed at fixed positions, the channel $\boldsymbol{C}_{B2R}$ can be accurately estimated during an initial calibration phase and is assumed to remain quasi-static over time [22], [23], [28].

where $\boldsymbol{A}_S \triangleq [\boldsymbol{a}_S(\theta_1), \boldsymbol{a}_S(\theta_2), \ldots, \boldsymbol{a}_S(\theta_K)]$, $\boldsymbol{A}_R \triangleq [\boldsymbol{a}_R(\tilde{\theta}_1), \boldsymbol{a}_R(\tilde{\theta}_2), \ldots, \boldsymbol{a}_R(\tilde{\theta}_K)]$, $\boldsymbol{\Lambda} \triangleq \mathrm{diag}\{\beta_k\}_{k=1}^K$, $\boldsymbol{D} \triangleq [\boldsymbol{\phi}(1)s(1), \ldots, \boldsymbol{\phi}(T)s(T)]$, and $\boldsymbol{N} \triangleq [\boldsymbol{n}(1), \boldsymbol{n}(2), \ldots, \boldsymbol{n}(T)]$.

III. Proposed Method

A. Initial DOA Estimation

Note that the measurement matrix $\boldsymbol{D}$ can be predefined at the BS and transmitted to the RIS through the RIS controller beforehand. To ensure accurate DOA estimation at the ASEs, the RIS measurement matrix $\boldsymbol{D}$ is usually defined as a DFT codebook [4], [21], [23]:

$$\boldsymbol{D} = [\boldsymbol{a}_R(\varphi_1), \boldsymbol{a}_R(\varphi_2), \ldots, \boldsymbol{a}_R(\varphi_T)] \in \mathbb{C}^{M_R\times T} \tag{6}$$

with the tth beam pointing to

$$\varphi_t = \arcsin\left(-1 + \frac{2t-1}{T}\right), \quad t = 1, \ldots, T. \tag{7}$$

During the tth sounding interval, the received signal $\boldsymbol{x}(t) \in \mathbb{C}^{M_S}$ at the ASEs can be expressed as

$$\boldsymbol{x}(t) = \boldsymbol{A}_S\boldsymbol{\Lambda}\boldsymbol{g}(\varphi_t) + \boldsymbol{n}(t) \tag{8}$$

where $\boldsymbol{g}(\varphi_t) \triangleq \boldsymbol{A}_R^H\boldsymbol{a}_R(\varphi_t) \in \mathbb{C}^{K\times 1}$.

Proposition 1: For a critically spaced ($d = \lambda/2$) ULA with M_R PREs, the kth entry of $\boldsymbol{g}(\varphi_t) \triangleq \boldsymbol{A}_R^H\boldsymbol{a}_R(\varphi_t)$ can be expressed in the Dirichlet closed form:

$$g_k(\varphi_t) = \frac{\sin\left[\frac{\pi M_R}{2}\left(\sin\varphi_t - \sin\tilde{\theta}_k\right)\right]}{\sin\left[\frac{\pi}{2}\left(\sin\varphi_t - \sin\tilde{\theta}_k\right)\right]}\cdot e^{j\frac{\pi(M_R-1)}{2}\left(\sin\varphi_t - \sin\tilde{\theta}_k\right)}. \tag{9}$$

Note that (9) attains its maximum magnitude of M_R when $\varphi_t = \tilde{\theta}_k$. In the sine-angle domain, the mainlobe spans a null-to-null width of $4/M_R$.

Proof: See Appendix I. ∎

Proposition 2: When the ASE steering vectors are (approximately) orthogonal, that is,

$$\boldsymbol{A}_S^H\boldsymbol{A}_S \approx \boldsymbol{I}_K \tag{10}$$

then, the instantaneous received power for RIS beam φ_t is

$$P(\varphi_t) \triangleq \|\boldsymbol{x}(t)\|_2^2 \approx \sum_{k=1}^{K}|\beta_k|^2\,|g_k(\varphi_t)|^2 + \|\boldsymbol{n}(t)\|_2^2. \tag{11}$$

Moreover, taking the statistical expectation over (11) gives

$$\mu(\varphi_t) = \mathbb{E}[P(\varphi_t)] \approx \sum_{k=1}^{K}|\beta_k|^2\,|g_k(\varphi_t)|^2 + M_S\sigma_n^2 \tag{12}$$

where $M_S\sigma_n^2$ is the constant noise floor across beams.

Proof: See Appendix II. ∎

From Proposition 2, provided that the RIS-domain DOAs are sufficiently separated ($|\sin\tilde{\theta}_i - \sin\tilde{\theta}_j| \geq 4/M_R$) so that mainlobes do not overlap, each resolvable target produces a distinct local maximum (spectral peak) at $\varphi_t \approx \tilde{\theta}_k$. Thus, coarse DOA estimation in the RIS domain amounts to selecting the K grid points at which the spatial spectrum $P(\varphi_t)$ attains its K largest local maxima. Denote the resulting coarse RIS-domain DOA estimates by $\{\hat{\varphi}_k^{(0)}\}_{k=1}^K$. From the relation:

Authorized licensed use limited to: Christopher Newport University. Downloaded on February 23,2026 at 12:29:37 UTC from IEEE Xplore. Restrictions apply.

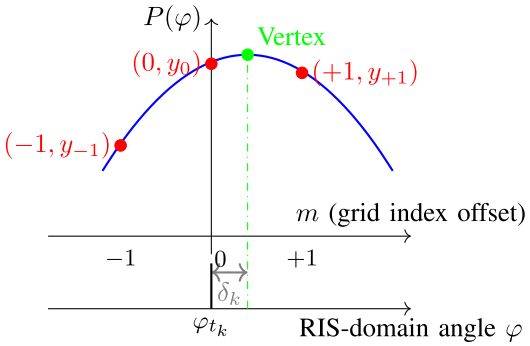

Fig. 2. Quadratic interpolation around the coarse spectral peak. The horizontal axis m denotes the local grid index offset from t_k, which corresponds to the RIS-domain angle φ_{t_k} in the lower axis. The vertex offset δ_k yields the refined peak position $\varphi_{t_k+\delta_k}$ prior to mapping to the ASE-domain DOA via (13).

$\sin\tilde{\theta}_k = \sin\theta_k - \sin\theta_{B2R}$, the coarse ASE-domain DOA estimates are given by

$$\widehat{\theta}_k^{(0)} = \arcsin\left(\sin\widehat{\varphi}_k^{(0)} + \sin\theta_{B2R}\right), \quad k = 1, \ldots, K. \tag{13}$$

B. Fine DOA Estimation via Quadratic Interpolation

Once the coarse RIS-domain DOA estimates $\{\widehat{\varphi}_k^{(0)}\}_{k=1}^K$ are obtained from the spatial spectrum $P(\varphi_t)$, their resolution is limited by the discrete beam grid spacing $\Delta_{\varphi_t} \triangleq \varphi_{t+1} - \varphi_t$. To achieve subgrid accuracy, we employ a standard quadratic interpolation around each coarse peak to refine the estimates [29].

Let t_k denote the grid index of the kth coarse estimate such that $\widehat{\varphi}_k^{(0)} = \varphi_{t_k}$. Denote the spatial spectrum samples at the peak and its two immediate neighbors as $y_{-1} \triangleq P(\varphi_{t_k-1})$, $y_0 \triangleq P(\varphi_{t_k})$, and $y_{+1} \triangleq P(\varphi_{t_k+1})$. We locally approximate the spectrum by a quadratic function

$$q(m) = am^2 + bm + c, \quad m \in \{-1, 0, 1\} \tag{14}$$

where $m = 0$ corresponds to φ_{t_k}, and $m = \pm 1$ correspond to the adjacent grid points.

Substituting $m = -1, 0, +1$ into (14) gives

$$\begin{cases} a - b + c = y_{-1} \\ c = y_0 \\ a + b + c = y_{+1} \end{cases} \tag{15}$$

which form a system of three linear equations in the unknowns (a, b, c). As shown in Fig. 2, solving (15) yields a closed-form expression for the vertex offset δ_k (in grid units) from t_k to the interpolated maximum

$$\delta_k = -\frac{b}{2a} = \frac{1}{2}\frac{y_{-1} - y_{+1}}{y_{-1} - 2\,y_0 + y_{+1}}. \tag{16}$$

Note that $|\delta_k| < 1$ under normal conditions, since the peak lies between its two neighbors.

The fine RIS-domain DOA estimate is then obtained as

$$\widehat{\varphi}_k^{(\text{fine})} = \varphi_{t_k} + \delta_k \Delta_{\varphi_{t_k}} \tag{17}$$

which yields subgrid accuracy in the sine-angle domain. Finally, the corresponding ASE-domain fine DOA estimates follow from the mapping in (13):

$$\widehat{\theta}_k^{(\text{fine})} = \arcsin\left(\sin\widehat{\varphi}_k^{(\text{fine})} + \sin\theta_{B2R}\right), \quad k = 1, \ldots, K. \tag{18}$$

Remark 1: Quadratic interpolation achieves an estimation accuracy significantly finer than the coarse grid spacing Δ_{φ_t}, especially at medium-to-high signal-to-noise ratio (SNR), while incurring negligible computational cost (see Sections IV and V). It effectively assumes that the spectrum shape near the peak is locally parabolic, which holds well for array beam patterns such as the Dirichlet kernel in Proposition 1.

The main steps of the proposed approach are summarized as follows.

IV. Performance Analysis

A. MSE Analysis of the Quadratic Interpolation Estimator

In general, obtaining a closed-form mse analysis for multiple DOA estimations is challenging. A commonly accepted approach is to focus on a single source and derive the corresponding mse to serve as a benchmark [30]. Consider the single-source case ($K = 1$) with the true RIS-domain DOA $\tilde{\theta}_1$ and its estimate φ_{t_1}. Let $g_1(\varphi_t)$ be defined as in (9). At $\varphi_t = \tilde{\theta}_1$, $|g_1(\tilde{\theta}_1)| = M_R$ and the mainlobe of $|g_1(\varphi_t)|^2$ is a squared Dirichlet kernel.

Proposition 3: The squared gain $|g_1(\varphi_t)|^2$ in the vicinity of φ_{t_1} admits the second-order Taylor expansion

$$|g_1(\varphi_t)|^2 \approx M_R^2 - \left[\frac{\pi^2\cos^2\varphi_{t_1}}{12} M_R^2\left(M_R^2 - 1\right)\right](\varphi_t - \varphi_{t_1})^2 \tag{19}$$

and the curvature term of the mean Bartlett spectrum $\mu(\varphi_t)$ at φ_{t_1} is

$$B = -\frac{1}{2}\mu''(\varphi_{t_1}) \approx \frac{|\beta_1|^2}{12}\pi^2\cos^2\varphi_{t_1} M_R^2\left(M_R^2 - 1\right). \tag{20}$$

Proof: See Appendix III. ∎

Proposition 4: Let $\text{mse}(\tilde{\theta}_1) \triangleq \mathbb{E}[(\varphi_{t_1} - \tilde{\theta}_1)^2]$, $\text{mse}(\theta_1) \triangleq \mathbb{E}[(\theta_1 - \widehat{\theta}_1)^2]$, we have

$$\text{mse}\left(\tilde{\theta}_1\right) \approx \frac{144 M_S\left(\sigma_n^4 + 2\sigma_n^2|\beta_1|^2 M_R^2\right)}{|\beta_1|^4\pi^4\cos^4\varphi_0 M_R^4\left(M_R^2 - 1\right)^2} \tag{21}$$

and

$$\text{MSE}(\theta_1) \approx \frac{144 M_S\left(\sigma_n^4 + 2\sigma_n^2|\beta_1|^2 M_R^2\right)}{|\beta_1|^4\pi^4\cos^2\varphi_{t_1}\left[1 - \left(\sin\varphi_{t_1} + \sin\theta_{B2R}\right)^2\right] M_R^4\left(M_R^2 - 1\right)^2}. \tag{22}$$

Proof: See Appendix IV. ∎

B. Complexity Analysis

In this section, we analyze the computational complexity of various methods used for estimating DOA in the context of a RIS-assisted sensing scenario depicted in Fig. 1. For comparison, we adopt two representative baseline methods: 1) The classical MUSIC method [22], which estimates DOAs via signal/noise subspace orthogonality and a grid search; 2) The ANM method [23], which formulates DOA estimation as a convex optimization problem solvable via semi-definite programming (SDP). Parameter settings follow the recommendations in their original works. The methods compared include MUSIC, ANM, initial coarse DOA estimation, and the

Authorized licensed use limited to: Christopher Newport University. Downloaded on February 23,2026 at 12:29:37 UTC from IEEE Xplore. Restrictions apply.

Method 1 Quadratic Interpolation Method

Input: Received signal: $\boldsymbol{X} \leftarrow [\boldsymbol{x}(1), \boldsymbol{x}(2), \ldots, \boldsymbol{x}(T)]$; Discrete RIS-domain scan grid: $\{\varphi_t\}_{t=1}^{T} \leftarrow \arcsin\left(-1+\frac{2t-1}{T}\right)$; BS-ASE geometric parameter: θ_{B2R}; Number of targets: K;

Compute RIS-domain spatial spectrum: $P(\varphi_t) \leftarrow \|\boldsymbol{x}(t)\|_2^2$;

Identify K peak indices of $P(\varphi_t)$: $\{t_k\}_{k=1}^{K}$;

for $k = 1$ to K **do**

  Extract three samples: $y_{-1} \leftarrow P(\varphi_{t_k-1})$, $y_0 \leftarrow P(\varphi_{t_k})$, $y_{+1} \leftarrow P(\varphi_{t_k+1})$;

  Compute subgrid vertex offset: $\delta_k \leftarrow \frac{1}{2} \cdot \frac{y_{-1}-y_{+1}}{y_{-1}-2y_0+y_{+1}}$;

  Refine RIS-domain DOA: $\widehat{\varphi}_k^{(\mathrm{fine})} \leftarrow \varphi_{t_k} + \delta_k \cdot (\varphi_{t_k+1} - \varphi_{t_k})$;

  Map to ASE-domain DOA: $\widehat{\theta}_k^{(\mathrm{fine})} \leftarrow \arcsin(\sin(\widehat{\varphi}_k^{(\mathrm{fine})}) + \sin\theta_{\mathrm{B2R}})$;

end for

return $\{\widehat{\theta}_k^{(\mathrm{fine})}\}$;

Output: Fine ASE-domain DOA estimates $\{\widehat{\theta}_k^{(\mathrm{fine})}\}_{k=1}^{K}$;

TABLE I
COMPARISON OF COMPLEXITY

Methods	Complexity
MUSIC	$\mathcal{O}\left(M_S^2 T + M_S^3 + g_\theta\left(M_S^2 + M_S\right)\left(M_S - K\right)\right)$
ANM	$\mathcal{O}\left(\left(M_S + M_R\right)^{3.5} + g_\theta\left(M_S M_R + M_S\right)\right)$
Initial	$\mathcal{O}\left(M_S T\right)$
Proposed	$\mathcal{O}\left(M_S T + K\right)$

proposed quadratic interpolation methods. The complexities of these methods are assessed based on the number of complex multiplications, providing an effective measure of their computational performance. According to the specific steps outlined in Method 1, the computational complexity of the proposed method consists primarily of two components: computing the RIS-domain spatial spectrum, which requires $\mathcal{O}(M_S T)$, and performing quadratic interpolation, which has a complexity of $\mathcal{O}(K)$. Table I outlines the complexity of different methods, where g_θ denotes the number of quantization grids for θ.

In Fig. 3(a)–(e), we analyze the complexity of various DOA estimation methods under different parameters. As the number of PREs M_R increases [Fig. 3(a)], the complexity of the ANM method rises sharply, indicating its sensitivity to M_R, while the proposed method maintains lower complexity. Similarly, Fig. 3(b) demonstrates that an increase in the number of ASEs M_S imposes greater computational burdens on the traditional MUSIC method compared to the proposed approach. Fig. 3(c) indicates that while the complexity of our method is sensitive to the number of snapshots T, it still achieves the lowest complexity overall. In Fig. 3(d), the complexity of our method remains nearly constant, as it is primarily influenced by $M_S T$ given that $T > K$. Finally, Fig. 3(e) shows that while the complexity of baseline methods increases with the quantization grid number g_θ, our method exhibits minimal impact since it does not require grid searching, thereby showcasing its reduced computational burden.

TABLE II
PARAMETER SETTING OF SIMULATIONS

Simulation parameters	Value	Unit
SNR	-10 $\sim$ 20	dB
K(number of targets)	1	-
T(number of snapshots)	256	-
λ(wavelength)	0.01	m
d(interval of array elements)	$\lambda/2$	m
M_S(number of ASEs)	4	-
M_R(number of PREs)	50	-
M_B(number of BS antennas)	50	-
M_c(number of Monte Carlo)	1000	-
θ(DOA at ASEs)	10.05	degree
θ_{B2R}(DOA at PREs)	50	degree
d_k(distance between RIS and target k)	7	m
d_{B2R}(distance between BS and RIS)	40	m
γ_k(radar cross section of target k)	10	dBsm
$\mathbb{G}$(DOA search space)	$\theta \in [9 : 0.1 : 11]$	degree

The above analyses theoretically demonstrate the impact of parameter variations on the complexity of different DOA estimation methods. Under various conditions, the proposed method consistently exhibits lower complexity compared to traditional MUSIC and ANM methods, highlighting its effectiveness and efficiency, particularly in large-scale RIS deployments. However, it is important to note that the actual execution time of these methods may be influenced by factors such as convergence rates and practical implementation details. To further validate the efficiency of the proposed method, we also include an assessment of the method's run time in our simulations.

V. SIMULATION RESULTS

To verify the effectiveness of our method, we conducted Monte Carlo experiments to evaluate its performance. The performance bound derived in Section IV-A is used as a benchmark. We define the root-mean-square error (RMSE) as

$$\mathrm{RMSE} = \sqrt{\frac{1}{K M_c}\sum_{i=1}^{M_c}\sum_{k=1}^{K}\left\|\hat{\theta}_{k,i} - \theta_k\right\|_2^2} \tag{23}$$

where M_c represents the number of Monte Carlo experiments, $\hat{\theta}_{k,i}$ denotes the estimated DOA of the kth target at ASEs in the ith experiment, whereas θ_k is the true DOA. Unless otherwise stated, see Table II for all simulation parameter settings, where SNR is defined as

$$\mathrm{SNR} \triangleq 10\log_{10}\left(\frac{\left\|\boldsymbol{A}_S \boldsymbol{\Lambda} \boldsymbol{A}_R^H \boldsymbol{D}\right\|_F^2}{M_S T \sigma_n^2}\right). \tag{24}$$

The simulations are implemented using MATLAB R2024a on a system with Windows 11, an i7-10700F processor, and 64 GB of RAM. The SDP defined in [23] is solved using the widely used MATLAB package CVX [31].

A. Simulations of Methods With Varying SNRs

In Figs. 4 and 5, we observe that the proposed method significantly outperforms the MUSIC and ANM methods at high SNR levels. Although traditional methods show improvement as SNR increases, they reach a performance limit largely due to their inability to effectively compensate for off-grid errors.

Authorized licensed use limited to: Christopher Newport University. Downloaded on February 23,2026 at 12:29:37 UTC from IEEE Xplore. Restrictions apply.

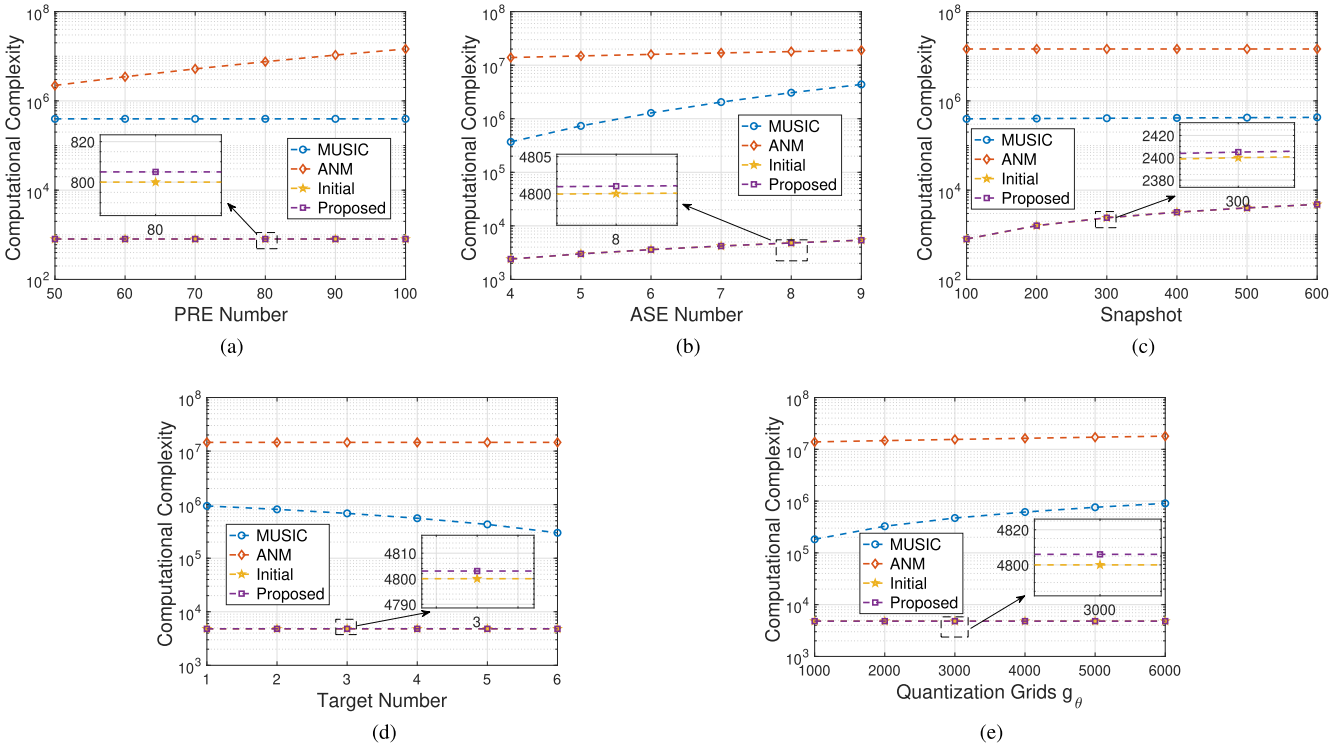

Fig. 3. Computational complexity comparison of different methods. (a) Complexity versus M_R when $T = 100$, $K = 5$, $g_\theta = 1800$, and $M_S = 8$. (b) Complexity versus M_S when $T = 600$, $K = 1$, $g_\theta = 6000$, and $M_R = 100$. (c) Complexity versus T when $M_R = 100$, $K = 5$, $g_\theta = 1800$, and $M_S = 8$. (d) Complexity versus K when $M_R = 100$, $T = 600$, $g_\theta = 1800$, and $M_S = 8$. (e) Complexity versus g_θ when $M_R = 100$, $T = 600$, $K = 6$, and $M_S = 8$.

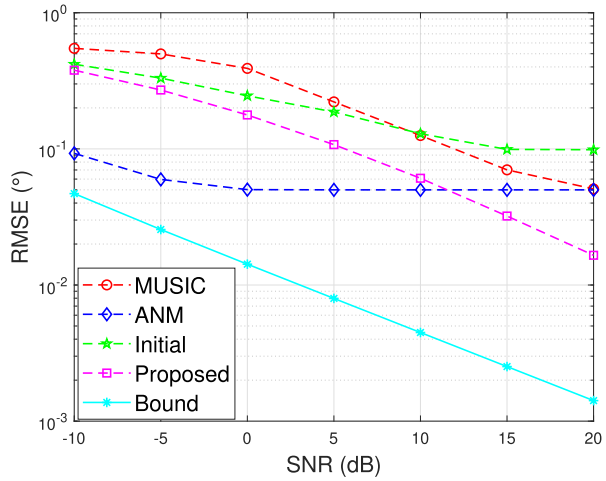

Fig. 4. RMSE versus SNR.

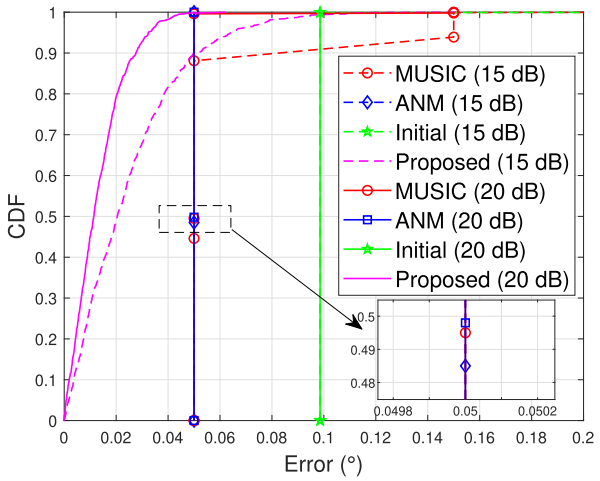

Fig. 5. DOA estimation error cdf versus SNR.

In contrast, our method achieves subgrid accuracy through quadratic interpolation, demonstrating its robustness and effectiveness in managing off-grid scenarios.

Regarding computational efficiency, Fig. 6 illustrates the average single-run time versus SNR, while Fig. 7 presents the cumulative distribution function (cdf) of single-run time. The proposed method consistently exhibits a substantially lower average run time compared to both MUSIC and ANM methods across all SNR levels. This reduced computational complexity renders the proposed method more suitable for real-time applications, further emphasizing its practical advantages.

In summary, the simulation results highlight the superior performance of the proposed method in both complexity and error compensation capabilities. This is particularly evident in high SNR environments, where traditional methods reach their limits due to challenges in addressing off-grid errors effectively.

B. Simulations of Methods With Varying Snapshots

In Figs. 8 and 9, we observe the DOA estimation performance of our method as a function of the number of snapshots T when SNR = 20 dB. As T increases, the baseline methods reach a performance limit in terms of RMSE, while the

Authorized licensed use limited to: Christopher Newport University. Downloaded on February 23,2026 at 12:29:37 UTC from IEEE Xplore. Restrictions apply.

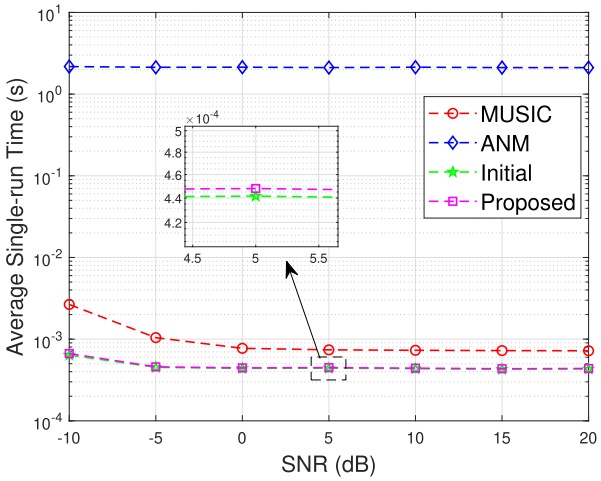

Fig. 6. Average single-run time versus SNR.

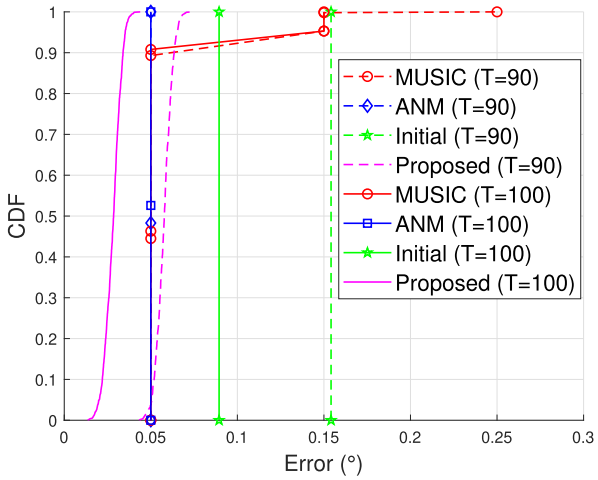

Fig. 9. DOA estimation error cdf versus snapshot.

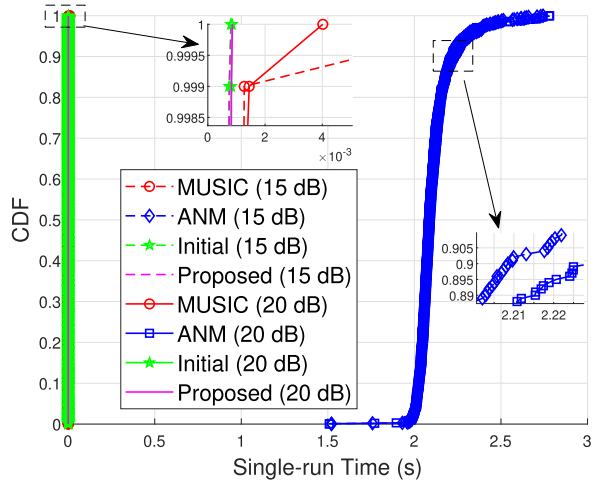

Fig. 7. Single-run time cdf versus SNR.

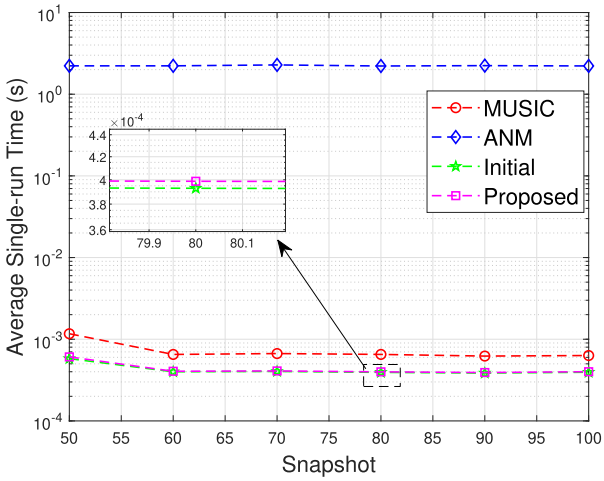

Fig. 10. Average single-run time versus snapshot.

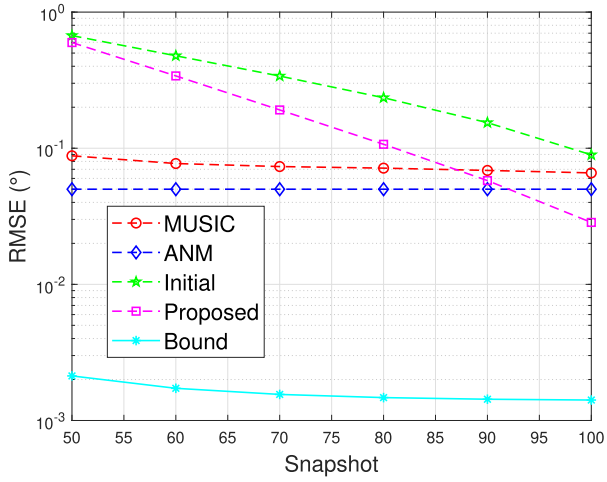

Fig. 8. RMSE versus snapshot.

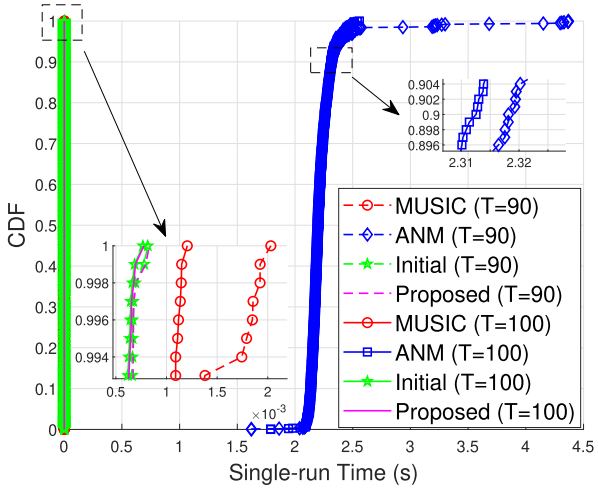

Fig. 11. Single-run time cdf versus snapshot.

proposed method consistently achieves lower RMSE values. This underscores its effectiveness in accurately estimating off-grid DOA.

Regarding computational efficiency, Fig. 10 illustrates the average single-run time versus T, and Fig. 11 presents the cdf of single-run time. Although the proposed method exhibits a slight increase in complexity due to the quadratic interpolation process compared to the initial DOA estimator, it still demonstrates significantly lower run times than both the MUSIC and ANM methods across all snapshot values. This highlights the

Authorized licensed use limited to: Christopher Newport University. Downloaded on February 23,2026 at 12:29:37 UTC from IEEE Xplore. Restrictions apply.

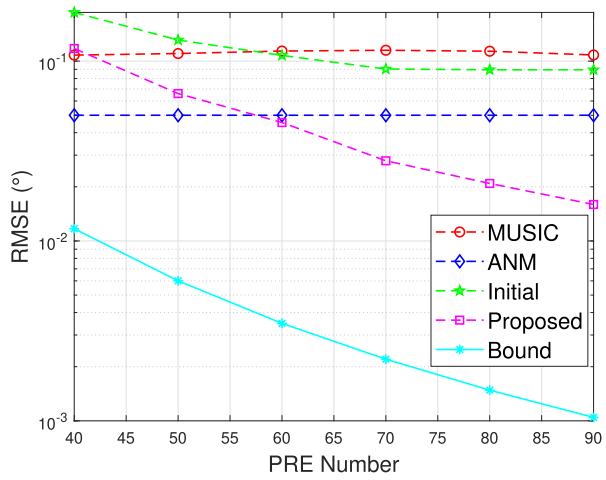

Fig. 12. RMSE versus M_R.

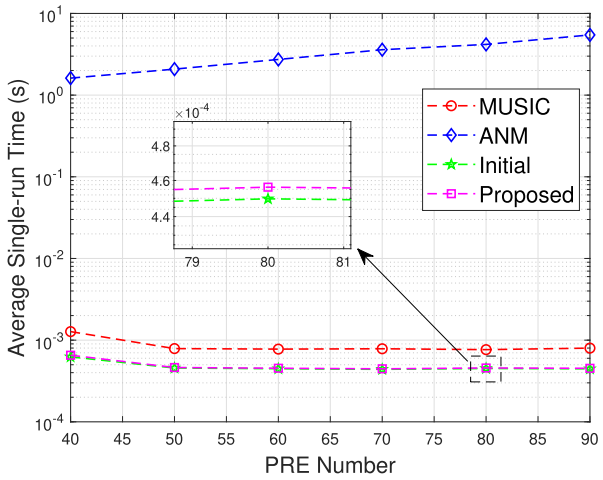

Fig. 14. Average single-run time versus M_R.

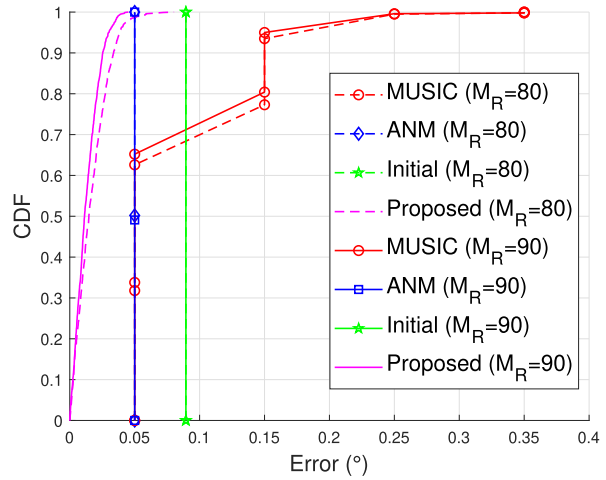

Fig. 13. DOA estimation error cdf versus M_R.

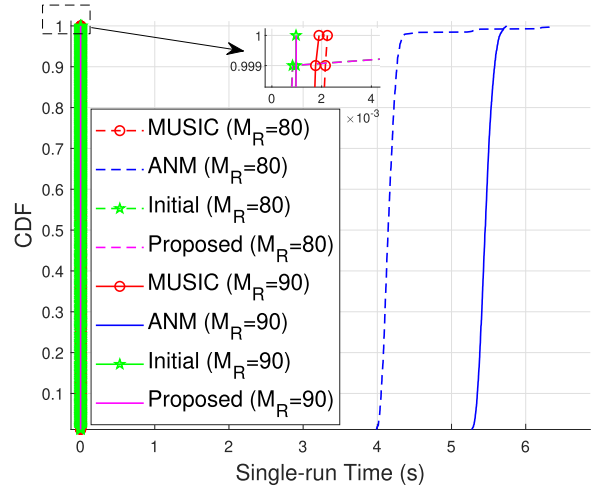

Fig. 15. Single-run time cdf versus M_R.

practicality of the proposed method, as its lower complexity does not compromise performance, making it particularly well-suited for applications that require rapid processing.

In summary, the simulation results affirm the proposed method's superior performance in both estimation accuracy and computational efficiency, especially when dealing with large numbers of snapshots.

C. Simulations of Methods With Varying PRE Numbers

In Figs. 12–15, we examine the DOA estimation performance of our method as a function of the PRE number M_R when $M_B = 4$, $T = 300$, and SNR $= 10$ dB. As M_R increases, baseline methods, particularly the ANM method, encounter significant challenges. The increase in the scale of SDP leads to an exponential rise in the method's run time, ultimately restricting its performance. In contrast, the proposed method consistently achieves lower RMSE values without an obvious increase in run time, demonstrating its robustness in accurately estimating off-grid DOA involving large PRE numbers.

Remark 2: When the number of ASEs is sufficiently large and the DOAs are exactly aligned with the predefined grid points, the resolution of baseline methods can improve markedly due to the enlarged aperture. Under this specific condition, such baselines may outperform the proposed method. However, in the more common off-grid scenarios, grid-based methods are subject to mismatch errors and thus suffer performance degradation, whereas the proposed method can accurately estimate arbitrary continuous-valued DOAs without discretization.

D. Simulations of Methods With Varying Target Numbers

In Figs. 16 and 17, we examine the DOA estimation performance of our method as a function of the target number K when $M_R = 100$, $M_S = 8$, $M_B = 8$, $T = 400$, and SNR $= 20$ dB. The DOA search space is set as $\mathbb{G} = \{\theta \in [0°: 0.1°:90°]\}$. Target DOAs at ASEs are randomly selected from the angular set $\{5.05°, 15.05°, 30.05°, 45.05°, 60.05°,$ and $75.05°\}$. As K increases, we find that the MUSIC method experiences a significant decline in performance. This is primarily due to its reliance on the degree-of-freedom (DOF) provided by the ASEs. In contrast, the initial estimation method shows little change in performance since its estimation capability depends on the DOF from PRE number. When $M_R \gg K$, variations in K have minimal impact on its performance. As K increases, the complexity of the signal's phase and amplitude variations also increases, which may lead

Authorized licensed use limited to: Christopher Newport University. Downloaded on February 23,2026 at 12:29:37 UTC from IEEE Xplore. Restrictions apply.

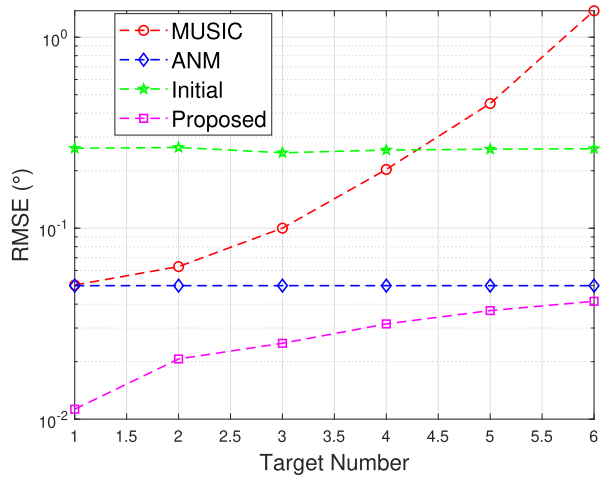

Fig. 16. RMSE versus K.

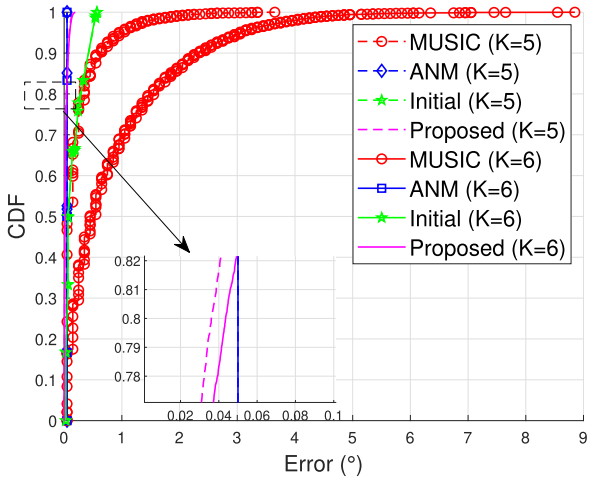

Fig. 17. DOA estimation error cdf versus K.

to inaccuracies in the interpolation model, particularly when there are significant changes in the relative positions of the targets. The proposed method, however, consistently maintains accurate performance across varying K. This robustness is attributed to its ability to effectively leverage additional information from the available PREs.

Moreover, the proposed method also exhibits superior stability in computational efficiency. Fig. 18 demonstrates that the average single-run time remains relatively constant across different target numbers. The cdf shown in Fig. 19 further highlights this efficiency, indicating that the proposed method consistently requires less computation time regardless of the target number.

E. Sensitivity Discussion of Methods

To evaluate the robustness of the proposed method under nonideal conditions, sensitivity analyses are conducted with respect to array mutual coupling, channel estimation error, phase distortion, and amplitude mismatch, as illustrated in Figs. 20–23. For the sensitivity analysis, the same baseline parameters as those used in Fig. 4 are adopted. Specifically, the SNR is fixed at 20 dB, and DOA search space is set as $\mathbb{G} = \{\theta \in [6° : 0.1° : 14°]\}$. In the nonideal cases, the perturbation ranges are configured as follows.

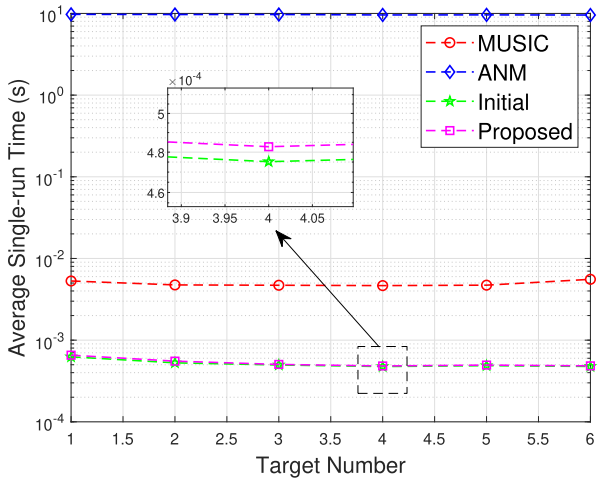

Fig. 18. Average single-run time versus K.

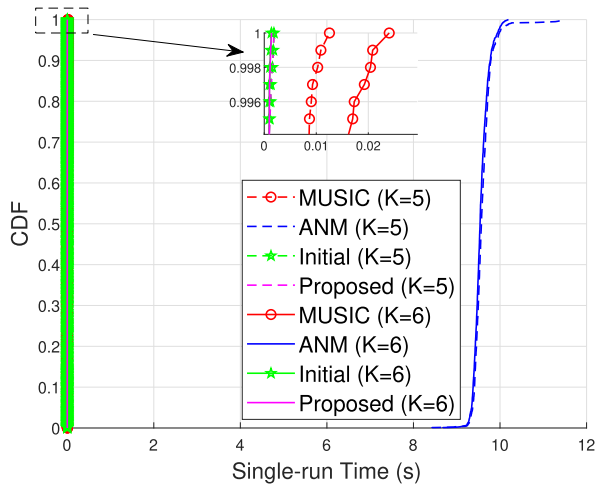

Fig. 19. Single-run time cdf versus K.

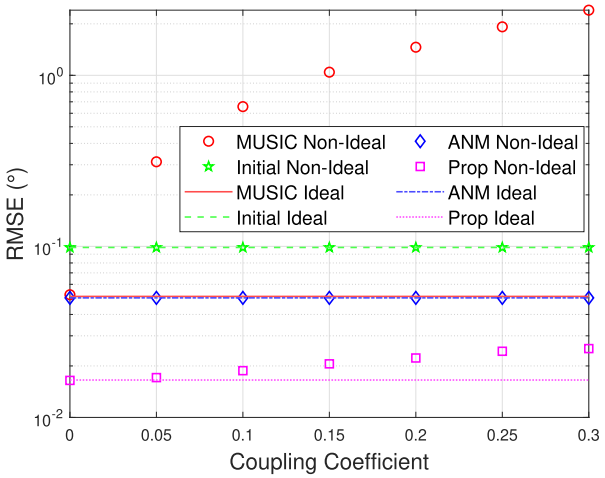

Fig. 20. Sensitivity of different DOA estimation methods to array mutual coupling.

1) *Array Mutual Coupling:* The coupling between adjacent elements is modeled by an exponentially decaying matrix

$$\boldsymbol{C}_R(m,n) = c^{|m-n|} \tag{25}$$

Authorized licensed use limited to: Christopher Newport University. Downloaded on February 23,2026 at 12:29:37 UTC from IEEE Xplore. Restrictions apply.

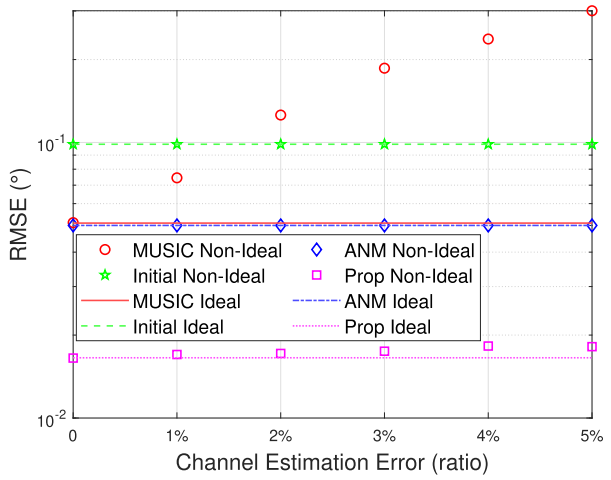

Fig. 21. Sensitivity of different DOA estimation methods to channel estimation error.

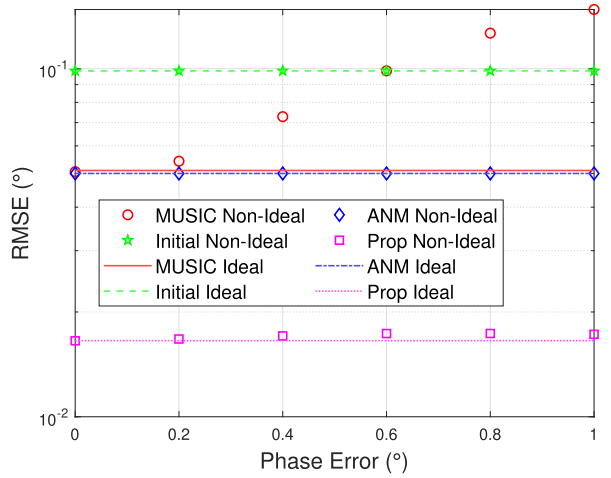

Fig. 22. Sensitivity of different DOA estimation methods to array phase error.

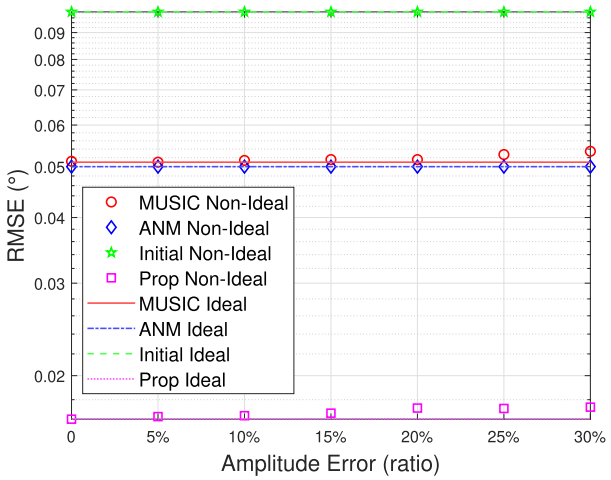

Fig. 23. Sensitivity of different DOA estimation methods to array amplitude error.

where $c \in [0, 0.3]$ denotes the adjacent-element coupling coefficient. The nonideal array response is expressed as

$$\boldsymbol{A}_{\text{nonideal}} = \boldsymbol{C}_R \boldsymbol{A}_{\text{ideal}}, \quad \boldsymbol{A}_{\text{ideal}} \in \{\boldsymbol{A}_{\text{R}}, \boldsymbol{A}_S\}. \tag{26}$$

2) *Channel Estimation Error:* The estimated channel matrix is modeled as

$$\widehat{\boldsymbol{H}} = \boldsymbol{H} + \Delta\boldsymbol{H}, \quad \|\Delta\boldsymbol{H}\|_F / \|\boldsymbol{H}\|_F = \rho \tag{27}$$

where $\boldsymbol{H} \in \{\boldsymbol{C}_{B2R}, \boldsymbol{C}_{\text{k}}\}$, $\rho \in [0, 5\%]$ represents the channel estimation error ratio.

3) *Phase Error:* Each array element is affected by a random phase distortion following a zero-mean Gaussian distribution:

$$\boldsymbol{q}_{\text{phase}} = \exp\left(j\sigma_\phi \boldsymbol{\epsilon}_\phi\right), \quad \boldsymbol{\epsilon}_\phi \sim \mathcal{N}(0, 1) \tag{28}$$

where σ_ϕ is the standard deviation of phase error ranging from 0° to 1°.

4) *Amplitude Error:* The amplitude imbalance of array elements is described by

$$\boldsymbol{q}_{\text{amp}} = 1 + \sigma_a \boldsymbol{\epsilon}_a, \quad \boldsymbol{\epsilon}_a \sim \mathcal{N}(0, 1) \tag{29}$$

where $\sigma_a \in [0, 0.3]$ controls the level of amplitude uncertainty.

In each sensitivity experiment, only one type of error factor is introduced while keeping all other conditions ideal. This ensures that the effect of each nonideal factor on the performance of different DOA estimation methods can be clearly and fairly assessed. As shown in Figs. 20–23, the proposed method and ANM maintain almost identical RMSE performance under nonideal conditions, whereas the conventional MUSIC method exhibits a significant degradation as the error level increases. For instance, when the mutual coupling coefficient grows from 0 to 0.3, the RMSE of MUSIC increases from approximately 0.05° to more than 1°, indicating nearly two orders of magnitude deterioration. In contrast, the proposed method and ANM show only marginal changes, with the RMSE variation remaining within 5% across all tested mutual coupling conditions. Furthermore, the proposed method consistently maintains an almost constant RMSE under different disturbance levels, including channel estimation error ratios (0%–5%), phase error standard deviations (0°–1°), and amplitude error ratios (0%–30%). These quantitative results demonstrate that the proposed method is one to two orders of magnitude more robust to model imperfections than the MUSIC method, thereby confirming its superior stability and practical reliability in realistic nonideal scenarios.

Remark 3: If calibration imperfections or coupling effects are significant, the proposed scheme can be integrated with existing calibration compensation and mutual coupling mitigation techniques [32], [33], [34].

F. Advantages of the Proposed Method

The advantages of the proposed method are summarized as follows.

1) The proposed method (DOF $= M_R - 1$) can estimate more targets than the MUSIC method (DOF $= M_S - 1$), particularly in large-scale RIS arrangements ($M_R \gg M_S$).
2) The proposed method exhibits significantly lower computational complexity, with runtime reduced by approximately 99.97% compared to ANM and 45.5% compared to MUSIC.

Authorized licensed use limited to: Christopher Newport University. Downloaded on February 23,2026 at 12:29:37 UTC from IEEE Xplore. Restrictions apply.

3) The proposed method is effective in addressing off-grid errors, thereby improving the accuracy of DOA estimation in practical scenarios. According to Fig. 7, when $T = 100$, the proposed method achieves an estimation error of approximately 0.04°, which represents a reduction of about 74% compared to MUSIC (0.15°) and about 20% compared to ANM (0.05°).

VI. Conclusion

In this article, we introduced a novel DOA estimation method based on quadratic interpolation, specifically designed for large-scale RIS deployments. Our results indicate that the proposed method outperforms traditional techniques such as MUSIC and ANM across several critical metrics. First, the proposed method demonstrates an enhanced capacity for estimating a greater number of targets, particularly in complex environments characterized by extensive RIS deployments. This advantage stems from the method's superior utilization of the available DOF provided by PREs. Second, our approach exhibits reduced computational complexity compared to both the MUSIC and ANM methods, rendering it a more efficient solution for real-time applications. This efficiency allows the proposed method to be readily adapted to various practical scenarios without sacrificing processing speed. At last, the proposed method effectively addresses off-grid errors, thereby improving the accuracy of DOA estimation. This capability is crucial for enhancing the reliability of systems reliant on precise localization information. In addition, the proposed DOA estimation framework also shows strong potential for practical implementation. It can be integrated into joint communication-sensing systems to facilitate beam alignment and localization, and combined with adaptive RIS control for real-time phase adjustment. These features highlight its applicability to future 6G intelligent wireless networks.

Appendix I
Proof of Proposition 1

The kth entry of $\boldsymbol{g}(\varphi_t)$ takes the form

$$g_k(\varphi_t) = \boldsymbol{a}_R^H\left(\tilde{\theta}_k\right)\boldsymbol{a}_R(\varphi_t) = \sum_{m=0}^{M_R-1} e^{jm\pi\left(\sin\varphi_t-\sin\tilde{\theta}_k\right)}. \tag{30}$$

Using the finite geometric series identity [35]

$$\sum_{m=0}^{M-1} e^{jm\alpha} = e^{j\alpha(M-1)/2}\frac{\sin(M\alpha/2)}{\sin(\alpha/2)} \tag{31}$$

and setting $\alpha = \pi(\sin\varphi_t - \sin\tilde{\theta}_k)$, (30) yields

$$g_k(\varphi_t) = \frac{\sin\left[\frac{\pi M_R}{2}\left(\sin\varphi_t-\sin\tilde{\theta}_k\right)\right]}{\sin\left[\frac{\pi}{2}\left(\sin\varphi_t-\sin\tilde{\theta}_k\right)\right]}\cdot e^{j\frac{\pi(M_R-1)}{2}\left(\sin\varphi_t-\sin\tilde{\theta}_k\right)}. \tag{32}$$

At $\varphi_t = \tilde{\theta}_k$, both the numerator and denominator vanish; applying L'Hôpital's rule [36]

$$\lim_{\varphi_t\to\tilde{\theta}_k}|g_k(\varphi_t)| = M_R \tag{33}$$

which proves that the peak magnitude equals the number of PREs. The first radiation null occurs when

$$\frac{\pi M_R}{2}\left(\sin\varphi_t-\sin\tilde{\theta}_k\right) = \pm\pi. \tag{34}$$

Therefore, in the sine-angle domain, the distance from the boresight to the first null is $\pm 2/M_R$, corresponding to a mainlobe width (null-to-null) of $4/M_R$. This completes the proof. ■

Appendix II
Proof of Proposition 2

From (8), the received vector is $\boldsymbol{x}(t) = \boldsymbol{s}(t) + \boldsymbol{n}(t)$, where we define the signal component $\boldsymbol{s}(t) \triangleq \boldsymbol{A}_S\boldsymbol{\Lambda}\boldsymbol{g}(\varphi_t)$. The instantaneous beam power is

$$P(\varphi_t) = \|\boldsymbol{s}(t)+\boldsymbol{n}(t)\|_2^2 = \underbrace{\|\boldsymbol{s}(t)\|_2^2}_{\text{signal power}} + \underbrace{\|\boldsymbol{n}(t)\|_2^2}_{\text{noise power}} + 2\Re\left\{\boldsymbol{s}^H(t)\boldsymbol{n}(t)\right\}. \tag{35}$$

Under the orthogonality assumption (10), we have

$$\|\boldsymbol{s}(t)\|_2^2 = \boldsymbol{g}^H(\varphi_t)\boldsymbol{\Lambda}^H\left(\boldsymbol{A}_S^H\boldsymbol{A}_S\right)\boldsymbol{\Lambda}\boldsymbol{g}(\varphi_t) \approx \sum_{k=1}^{K}|\beta_k|^2|g_k(\varphi_t)|^2. \tag{36}$$

Since $n_m(t) \overset{\text{i.i.d.}}{\sim} \mathcal{CN}(0,\sigma_n^2)$, $\mathbb{E}[\|\boldsymbol{n}(t)\|_2^2] = M_S\sigma_n^2$. The cross term $2\Re\{\boldsymbol{s}^H(t)\boldsymbol{n}(t)\}$ has zero mean because $\boldsymbol{n}(t)$ is zero-mean and independent of $\boldsymbol{s}(t)$. Taking expectations over (35) thus yields (12). ■

Appendix III
Proof of Proposition 3

From Proposition 1, in the single-source case $K = 1$ with $\varphi_{t_1} = \tilde{\theta}_1$

$$|g_1(\varphi_t)|^2 = \frac{\sin^2\left[\frac{\pi M_R}{2}\left(\sin\varphi_t-\sin\varphi_{t_1}\right)\right]}{\sin^2\left[\frac{\pi}{2}\left(\sin\varphi_t-\sin\varphi_{t_1}\right)\right]}. \tag{37}$$

Let $\delta \triangleq \varphi_t - \varphi_{t_1}$. Using the first-order Taylor expansion of $\sin(\cdot)$ at φ_{t_1} [37]

$$\sin\left(\varphi_{t_1}+\delta\right) = \sin\varphi_{t_1} + \delta\cos\varphi_{t_1} - \frac{1}{2}\delta^2\sin\varphi_{t_1} + \mathcal{O}\left(\delta^3\right) \tag{38}$$

we obtain, for $|\delta| \ll 1$ (mainlobe region)

$$\sin\varphi_t - \sin\varphi_{t_1} \approx \delta\cos\varphi_{t_1} \tag{39}$$

since the δ^2 and higher order terms are negligible in the curvature calculation. Let $x \triangleq \pi/2\delta\cos\varphi_{t_1}$, we can rewrite (37) as

$$|g_1(\varphi_t)|^2 = \frac{\sin^2(M_R x)}{\sin^2(x)}. \tag{40}$$

Using the small-angle expansions [37] $\sin(M_R x) \approx M_R x - (M_R x)^3/6$, $\sin(x) \approx x - x^3/6$ and straightforward division yields $\sin(M_R x)/\sin(x) \approx M_R[1-(M_R^2-1)x^2/6] + \mathcal{O}(x^4)$. Squaring and keeping only the x^2 term results in

$$|g_1(\varphi_t)|^2 \approx M_R^2\left[1-\frac{\left(M_R^2-1\right)x^2}{3}\right] + \mathcal{O}\left(x^4\right). \tag{41}$$

Authorized licensed use limited to: Christopher Newport University. Downloaded on February 23,2026 at 12:29:37 UTC from IEEE Xplore. Restrictions apply.

Substituting $x^2 = (\pi^2 \cos^2 \varphi_{t_1})/4(\varphi - \varphi_{t_1})^2$ into (41) produces the expansion (19). For the mean spectrum $\mu(\varphi_t) \approx |\beta_1|^2 |g_1(\varphi_t)|^2 + M_S \sigma_n^2$, the constant noise floor does not contribute to $\mu''(\varphi_{t_1})$, hence the second derivative

$$\mu''\left(\varphi_{t_1}\right) \approx -2 \cdot \frac{\pi^2 \cos^2 \varphi_{t_1}}{12} M_R^2 \left(M_R^2 - 1\right) |\beta_1|^2 . \tag{42}$$

By definition $B \triangleq -1/2\mu''(\varphi_{t_1})$, we can obtain (20). This completes the proof. ■

Appendix IV
Proof of Proposition 4

At $\varphi_t = \varphi_{t_1}$, the instantaneous received vector in (4) can be approximated as

$$\boldsymbol{x}\left(t_1\right) \approx \beta_1 M_R \boldsymbol{a}_S\left(\theta_1\right) + \boldsymbol{n}\left(t_1\right) \tag{43}$$

where $\|\boldsymbol{a}_S(\theta_1)\|_2^2 = M_S$, and $\boldsymbol{n}(t_1) \sim \mathcal{CN}(\boldsymbol{0}, \sigma_n^2 \boldsymbol{I}_{M_S})$. Subsequently, the received power at φ_{t_1} based on one snapshot is given by

$$\begin{aligned} P\left(\varphi_{t_1}\right) &= \left\|\beta_1 M_R \boldsymbol{a}_S\left(\theta_1\right) + \boldsymbol{n}\left(t_1\right)\right\|_2^2 \\ &= \|\boldsymbol{s}_1\|_2^2 + \|\boldsymbol{n}\left(t_1\right)\|_2^2 + 2\Re\left\{\boldsymbol{s}_1^H \boldsymbol{n}\left(t_1\right)\right\} \end{aligned} \tag{44}$$

where $\boldsymbol{s}_1 \triangleq \beta_1 M_R \boldsymbol{a}_S(\theta_1)$. Note that $\|\boldsymbol{s}_1\|_2^2 = |\beta_1|^2 M_R^2 M_S$ is constant and the random variable $\boldsymbol{s}_1^H \boldsymbol{n}(t_1)$ is zero-mean complex Gaussian with variance

$$\begin{aligned} \operatorname{Var}\left[\boldsymbol{s}_1^H \boldsymbol{n}\left(t_1\right)\right] &= \sigma_n^2 \|\boldsymbol{s}_1\|_2^2 \\ &= \sigma_n^2 |\beta_1|^2 M_R^2 \left\|\boldsymbol{a}_S\left(\theta_1\right)\right\|_2^2 \\ &= \sigma_n^2 |\beta_1|^2 M_R^2 M_S. \end{aligned} \tag{45}$$

Since each entry of $\boldsymbol{n}(t_1)$ is i.i.d. $\mathcal{CN}(0, \sigma_n^2)$, $\|\boldsymbol{n}(t_1)\|^2/\sigma_n^2$ follows a chi-square distribution with $2M_S$ degrees of freedom, yielding

$$\operatorname{Var}\left[\left\|\boldsymbol{n}\left(t_1\right)\right\|_2^2\right] = M_S \sigma_n^4. \tag{46}$$

Therefore, we have

$$\sigma_P^2 \triangleq \operatorname{Var}\left[P\left(\varphi_{t_1}\right)\right] = M_S \sigma_n^4 + 2\sigma_n^2 |\beta_1|^2 M_R^2 M_S. \tag{47}$$

Subsequently, according to the generic bound of parabolic peak approximation [38], we have

$$\operatorname{mse}\left(\varphi_{t_1}\right) \approx \frac{\sigma_P^2}{B^2} = \frac{144 M_S \left(\sigma_n^4 + 2\sigma_n^2 |\beta_1|^2 M_R^2\right)}{|\beta_1|^4 \pi^4 \cos^4 \varphi_{t_1} M_R^4 \left(M_R^2 - 1\right)^2}. \tag{48}$$

Let $f(\varphi_t) \triangleq \arcsin(\sin \varphi_t + \sin \theta_{B2R})$, so that $\widehat{\theta}_1 = f(\varphi_{t_1})$. When the small error $(\widehat{\theta}_1 - \varphi_{t_1})$ is approximated by its first-order linear expansion, we have

$$\begin{aligned} &\operatorname{mse}\left(\theta_1\right) \\ &\approx \left[f'\left(\varphi_{t_1}\right)\right]^2 \cdot \operatorname{mse}\left(\tilde{\theta}_1\right) \\ &= \frac{144 M_S \left(\sigma_n^4 + 2\sigma_n^2 |\beta_1|^2 M_R^2\right)}{|\beta_1|^4 \pi^4 \cos^2 \varphi_{t_1} \left[1 - \left(\sin \varphi_{t_1} + \sin \theta_{B2R}\right)^2\right] M_R^4 \left(M_R^2 - 1\right)^2}. \end{aligned} \tag{49}$$

This completes the proof. ■

References

[1] H. Yang et al., "Intelligent computation offloading for joint communication and sensing-based vehicular networks," *IEEE Trans. Wireless Commun.*, vol. 23, no. 4, pp. 3600–3616, Apr. 2024.

[2] X. Shi, X. Zhang, J. Li, M. Sun, T. Q. S. Quek, and H. C. So, "Direct localization of high-order QAM sources with multiple anchors: Dual atomic norm minimization framework," *IEEE Trans. Wireless Commun.*, early access, Aug. 25, 2025, doi: 10.1109/TWC.2025.3599530.

[3] Z. Chen, L. Huang, H. C. So, H. Jiang, X. Y. Zhang, and J. Wang, "Deep reinforcement learning over RIS-assisted integrated sensing and communication: Challenges and opportunities," *IEEE Veh. Technol. Mag.*, vol. 20, no. 3, pp. 97–105, Sep. 2025.

[4] X. Shi, X. Zhang, T. Q. S. Quek, and H. C. So, "Semi-passive IRS-aided DOA estimation: Weighted ESPRIT approach," *IEEE Wireless Commun. Lett.*, vol. 14, no. 8, pp. 2366–2370, Aug. 2025.

[5] H. Pan, J. Pan, X. Zhang, and Y. Wang, "Co-prime sampling-based gridless time-delay estimation for ground penetrating radar system with enhanced single measurement vector," *IEEE Geosci. Remote Sens. Lett.*, vol. 22, pp. 1–5, 2025.

[6] Z. Chen, M.-M. Zhao, M. Li, F. Xu, Q. Wu, and M.-J. Zhao, "Joint location sensing and channel estimation for IRS-aided mmWave ISAC systems," *IEEE Trans. Wireless Commun.*, vol. 23, no. 9, pp. 11985–12002, Sep. 2024.

[7] F. Wen, J. Shi, G. Gui, C. Yuen, H. Sari, and F. Adachi, "Joint DOD and DOA estimation for NLOS target using IRS-aided bistatic MIMO radar," *IEEE Trans. Veh. Technol.*, vol. 73, no. 10, pp. 15798–15802, Oct. 2024.

[8] H. Sun, L. Zhu, W. Mei, and R. Zhang, "Power-measurement-based channel autocorrelation estimation for IRS-assisted wideband communications," *IEEE Trans. Wireless Commun.*, vol. 24, no. 6, pp. 4647–4662, Jun. 2025.

[9] X. Song, X. Qin, J. Xu, and R. Zhang, "Cramér–Rao bound minimization for IRS-enabled multiuser integrated sensing and communications," *IEEE Trans. Wireless Commun.*, vol. 23, no. 8, pp. 9714–9729, Aug. 2024.

[10] X. Shao, C. You, and R. Zhang, "Intelligent reflecting surface aided wireless sensing: Applications and design issues," *IEEE Wireless Commun.*, vol. 31, no. 3, pp. 383–389, Jun. 2024.

[11] M. Hua, G. Chen, K. Meng, S. Ma, C. Yuen, and H. C. So, "3D multi-target localization via intelligent reflecting surface: Protocol and analysis," *IEEE Trans. Wireless Commun.*, vol. 23, no. 11, pp. 16527–16543, Nov. 2024.

[12] D. Li, Z. Yang, N. Zhao, Z. Wu, and T. Q. S. Quek, "NOMA aided secure transmission for IRS-ISAC," *IEEE Trans. Wireless Commun.*, vol. 23, no. 9, pp. 10911–10925, Sep. 2024.

[13] X. Shao, C. You, W. Ma, X. Chen, and R. Zhang, "Target sensing with intelligent reflecting surface: Architecture and performance," *IEEE J. Sel. Areas Commun.*, vol. 40, no. 7, pp. 2070–2084, Jul. 2022.

[14] M. A. Haider, Y. D. Zhang, and E. Aboutanios, "Channel estimation and prediction in wireless communications assisted by semi-passive RIS," in *Proc. IEEE Int. Conf. Acoust., Speech Signal Process. (ICASSP)*, Apr. 2024, pp. 8601–8605.

[15] Q. Peng, Q. Wu, W. Chen, S. Ma, M.-M. Zhao, and O. A. Dobre, "Semi-passive intelligent reflecting surface-enabled sensing systems," *IEEE Trans. Commun.*, vol. 72, no. 12, pp. 7674–7688, Dec. 2024.

[16] X. Shi, X. Zhang, Y. Qian, and M. Ahmad, "Closed-form rectilinear emitters localization with multiple sensor arrays: Phase alignment and optimal weighted least-square method," *IEEE Sensors J.*, vol. 23, no. 7, pp. 7266–7278, Apr. 2023.

[17] X. Shi, X. Zhang, Y. Sun, and Y. Qian, "Direct position determination of non-circular signals for distributed antenna arrays: Optimal weight and polynomial rooting approach," *IEEE Signal Process. Lett.*, vol. 31, pp. 256–260, 2024.

[18] J. Cao, X. Zhang, H. Hao, and X. Shi, "Noncircular signal tracking with distributed passive arrays: Combining data fusion and extended Kalman filter," *IEEE Sensors J.*, vol. 24, no. 1, pp. 757–768, Jan. 2024.

[19] X. Shi, X. Zhang, Y. Sun, Y. Qian, and J. Cao, "Multiple sources localization with 2D-DFT under distributed massive antenna arrays," *Signal Process.*, vol. 217, Apr. 2024, Art. no. 109340.

Authorized licensed use limited to: Christopher Newport University. Downloaded on February 23,2026 at 12:29:37 UTC from IEEE Xplore. Restrictions apply.

[20] X. Shi, X. Zhang, and H. Zeng, "Direct position determination of non-circular sources for multiple arrays via weighted Euler ESPRIT data fusion method," *Appl. Sci.*, vol. 12, no. 5, p. 2503, Feb. 2022.
[21] R. Li, X. Shao, S. Sun, M. Tao, and R. Zhang, "Beam scanning for integrated sensing and communication in IRS-aided mmWave systems," in *Proc. IEEE 24th Int. Workshop Signal Process. Adv. Wireless Commun. (SPAWC)*, Shanghai, China, Sep. 2023, pp. 196–200.
[22] M. Hua, Q. Wu, W. Chen, Z. Fei, H. C. So, and C. Yuen, "Intelligent reflecting surface-assisted localization: Performance analysis and algorithm design," *IEEE Wireless Commun. Lett.*, vol. 13, no. 1, pp. 84–88, Jan. 2024.
[23] R. Li, S. Sun, and M. Tao, "Atomic norm minimization-based DoA estimation for IRS-assisted sensing systems," *IEEE Wireless Commun. Lett.*, vol. 13, no. 10, pp. 2672–2676, Oct. 2024.
[24] C. Zhou, Y. Gu, Z. Shi, and Y. D. Zhang, "Off-grid direction-of-arrival estimation using coprime array interpolation," *IEEE Signal Process. Lett.*, vol. 25, no. 11, pp. 1710–1714, Nov. 2018.
[25] H. Huang, H. C. So, and A. M. Zoubir, "Off-grid direction-of-arrival estimation using second-order Taylor approximation," *Signal Process.*, vol. 196, Jul. 2022, Art. no. 108513.
[26] C. Hu, R. Zhang, G. Chen, X. Luo, X. Guan, and C. Yuen, "Reconfigurable coding design for programmable metasurface-based DOA estimation via Riemannian manifold optimization," *IEEE Wireless Commun. Lett.*, early access, Aug. 12, 2025, doi: 10.1109/LWC.2025.3598026.
[27] R. Zhang, B. Shim, and W. Wu, "Direction-of-arrival estimation for large antenna arrays with hybrid analog and digital architectures," *IEEE Trans. Signal Process.*, vol. 70, pp. 72–88, 2022.
[28] S. Buzzi, E. Grossi, M. Lops, and L. Venturino, "Foundations of MIMO radar detection aided by reconfigurable intelligent surfaces," *IEEE Trans. Signal Process.*, vol. 70, pp. 1749–1763, 2022.
[29] L. Pallotta, G. Giunta, and A. Farina, "DOA refinement through complex parabolic interpolation of a sparse recovered signal," *IEEE Signal Process. Lett.*, vol. 28, pp. 274–278, 2021.
[30] R. Cao, B. Liu, F. Gao, and X. Zhang, "A low-complex one-snapshot DOA estimation algorithm with massive ULA," *IEEE Commun. Lett.*, vol. 21, no. 5, pp. 1071–1074, May 2017.
[31] M. Grant, S. Boyd, and Y. Ye, "CVX: MATLAB software for disciplined convex programming," Stanford Univ., Stanford, CA, USA, 2014.
[32] Q. Li, M. El-Hajjar, C. Xu, J. An, C. Yuen, and L. Hanzo, "Stacked intelligent metasurfaces for holographic MIMO-aided cell-free networks," *IEEE Trans. Commun.*, vol. 72, no. 11, pp. 7139–7151, Nov. 2024.
[33] Q. Li, M. El-Hajjar, K. Cao, C. Xu, H. Haas, and L. Hanzo, "Holographic metasurface-based beamforming for multi-altitude LEO satellite networks," *IEEE Trans. Wireless Commun.*, vol. 24, no. 4, pp. 3103–3116, Apr. 2025.
[34] Q. Li, M. El-Hajjar, Y. Sun, and L. Hanzo, "Performance analysis of reconfigurable holographic surfaces in the near-field scenario of cell-free networks under hardware impairments," *IEEE Trans. Wireless Commun.*, vol. 23, no. 9, pp. 11972–11984, Sep. 2024.
[35] A. Pott, *Finite Geometry and Character Theory*. Cham, Switzerland: Springer, 2006.
[36] C. M. Lee, "Generalizations of l'hôpital's rule," *Proc. Amer. Math. Soc.*, vol. 66, no. 2, pp. 315–320, 1977.
[37] D. Hirst, "Series, Taylor—Maclaurin series," in *Mathematics for Chemists*. Cham, Switzerland: Springer, 1976, pp. 139–152.
[38] P. Stoica et al., *Spectral Analysis of Signals*, vol. 452. Upper Saddle River, NJ, USA: Prentice-Hall, 2005.

Qi Yuan received the M.S. degree in information and communication engineering with Nanjing University of Aeronautics and Astronautics, Nanjing, China, in 2015, where he is currently pursuing the Ph.D. degree in information and communication engineering.

His research interests include signal and information processing and radiation source localization.

Xinlei Shi (Graduate Student Member, IEEE) received the B.S. degree in electronic information science and technology from Jiangsu University of Science and Technology, Zhenjiang, China, in 2021. He is currently pursuing the Ph.D. degree in information and communication engineering with Nanjing University of Aeronautics and Astronautics, Nanjing, China.

His research interests include signal and information processing and radiation source localization.

Xiaofei Zhang received the M.S. degree in electrical engineering from Wuhan University, Wuhan, China, in 2001, and the Ph.D. degree in communication and information systems from Nanjing University of Aeronautics and Astronautics, Nanjing, China, in 2005.

He is currently a Professor with the College of electronic and information engineering, Nanjing University of Aeronautics and Astronautics. His research interests include array signal processing, communication signal processing, and multidimension systems.

Fuhui Zhou (Senior Member, IEEE) is currently a Full Professor with Nanjing University of Aeronautics and Astronautics, Nanjing, China, where he is also with the Key Laboratory of Dynamic Cognitive System of Electromagnetic Spectrum Space. He has published more than 200 articles in internationally renowned journals and conferences in the field of communications. He has been selected for one ESI hot paper and 13 ESI highly cited papers. His research interests include cognitive radio, cognitive intelligence, knowledge graph, edge computing, and resource allocation.

Prof. Zhou has received four Best Paper Awards at international conferences, such as IEEE Globecom and IEEE ICC. He was awarded the 2021 Most Cited Chinese Researchers by Elsevier, the Stanford World's Top 2% Scientists, the IEEE ComSoc Asia-Pacific Outstanding Young Researcher and Young Elite Scientist Award of China, and the URSI GASS Young Scientist. He serves as an Editor for IEEE TRANSACTIONS ON COMMUNICATIONS, IEEE SYSTEMS JOURNAL, IEEE WIRELESS COMMUNICATIONS LETTERS, IEEE ACCESS, and *Physical Communication*.

Authorized licensed use limited to: Christopher Newport University. Downloaded on February 23,2026 at 12:29:37 UTC from IEEE Xplore. Restrictions apply.